SUPPLEMENTARY INFORMATION

Three-dimensional structure and flexibility of a membrane-coating module of the nuclear pore complex

Martin Kampmann and Günter Blobel

Laboratory of Cell Biology, Howard Hughes Medical Institute, The Rockefeller University, 1230 York Avenue, New York, NY 10065, USA

blobel@rockefeller.edu

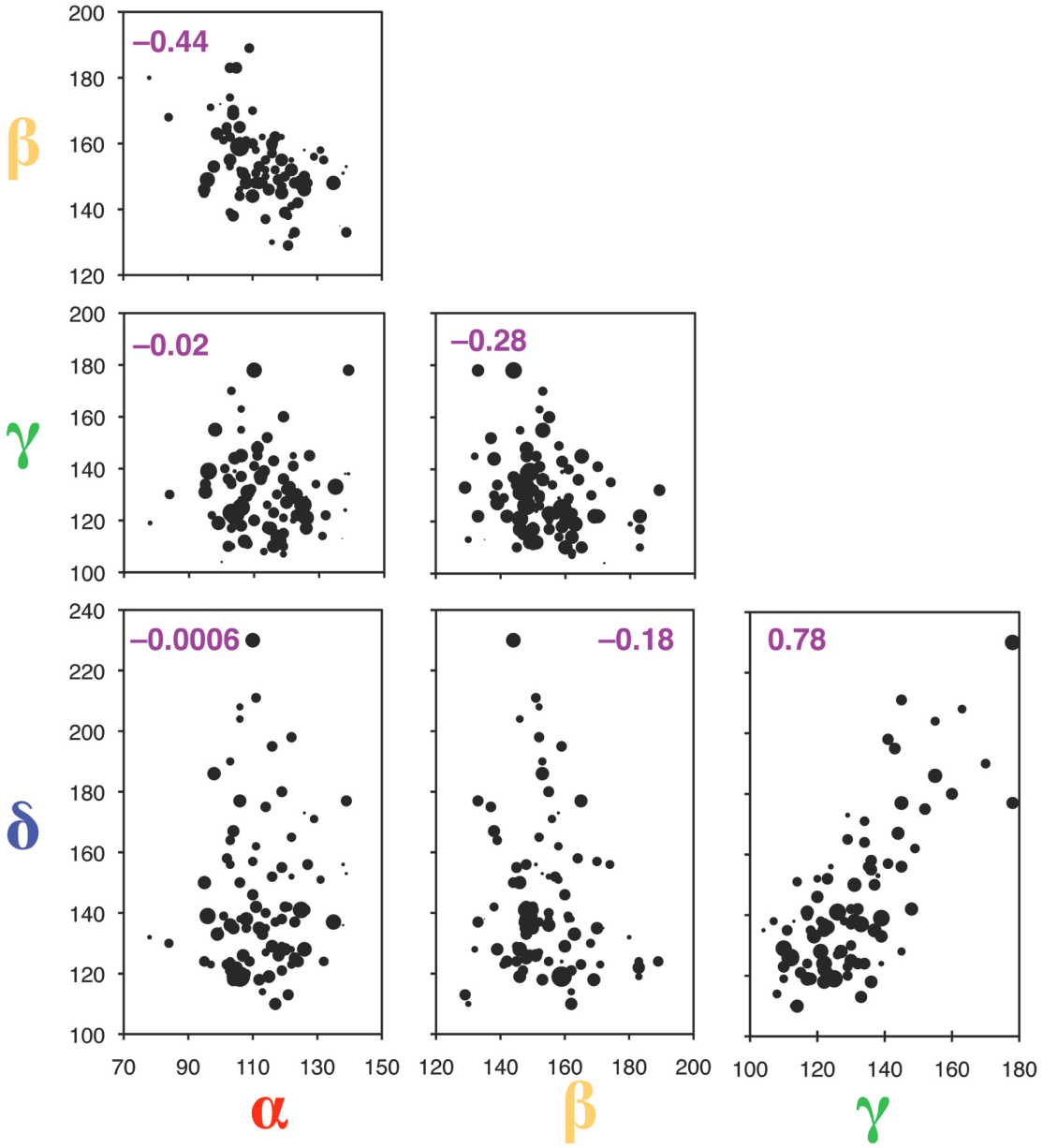

Supplementary Figure 1 Angles between particle segments, as defined in Figure 3a. All binary combinations of angles α, β, γ and δ are plotted; each marker represents two angles for a particle class. Marker area is proportional to class size. Particle-based correlation coefficients are indicated in purple.

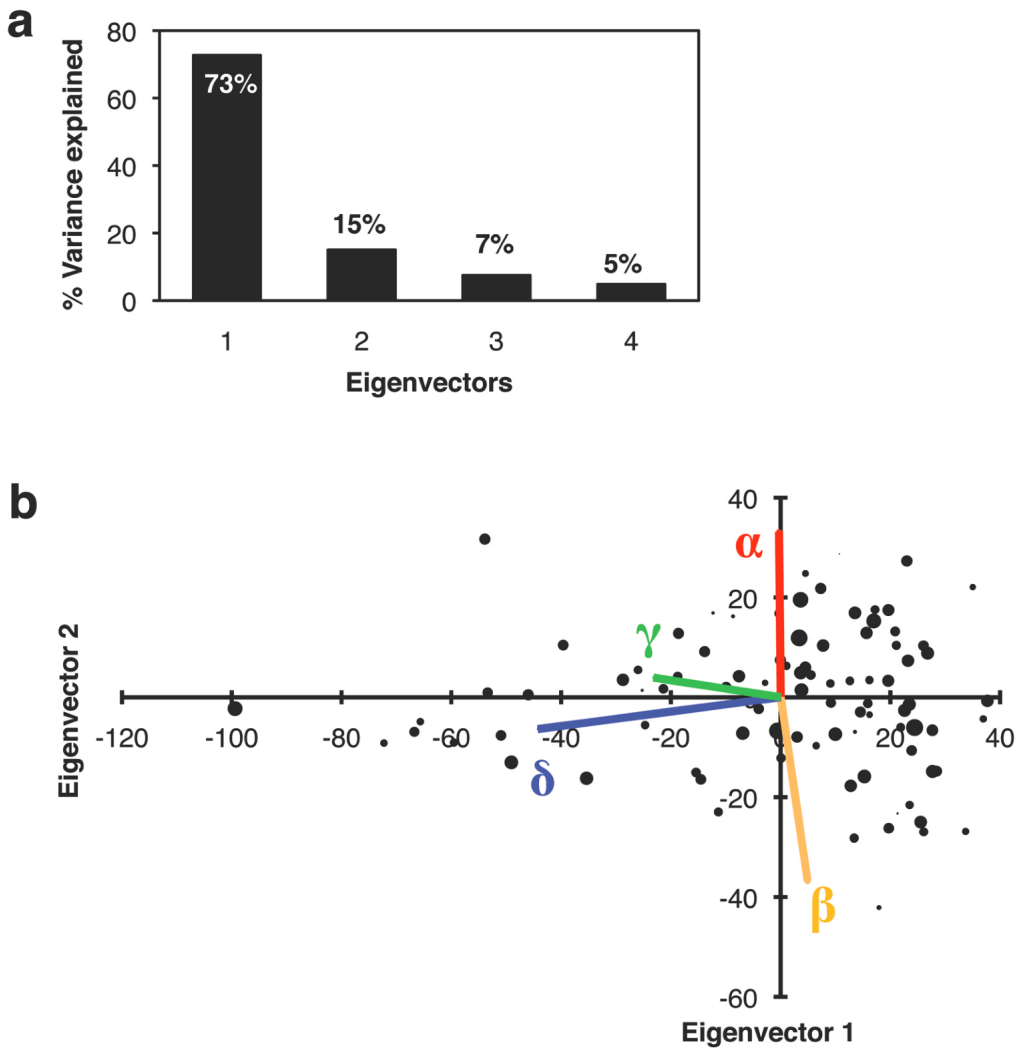

Supplementary Figure 2 Principle component analysis (PCA) of the variation of angles α, β, γ and δ between particle segments (see also Fig. 3 and Supplementary Fig. 1). (**a**) Eigenvector 1 explains 73% of the variance; the remaining three eigenvectors explain the residual 27% of the variance. (**b**) Biplot: The black dots correspond to the original data projected onto the plane defined by the first two eigenvectors. The projections of the four original dimensions (angles) onto this plane are indicated by colored lines. Eigenvector 1 represents mainly the correlated variation in γ and δ. Eigenvector 2 represents mainly the anti-correlated variation in α and β.

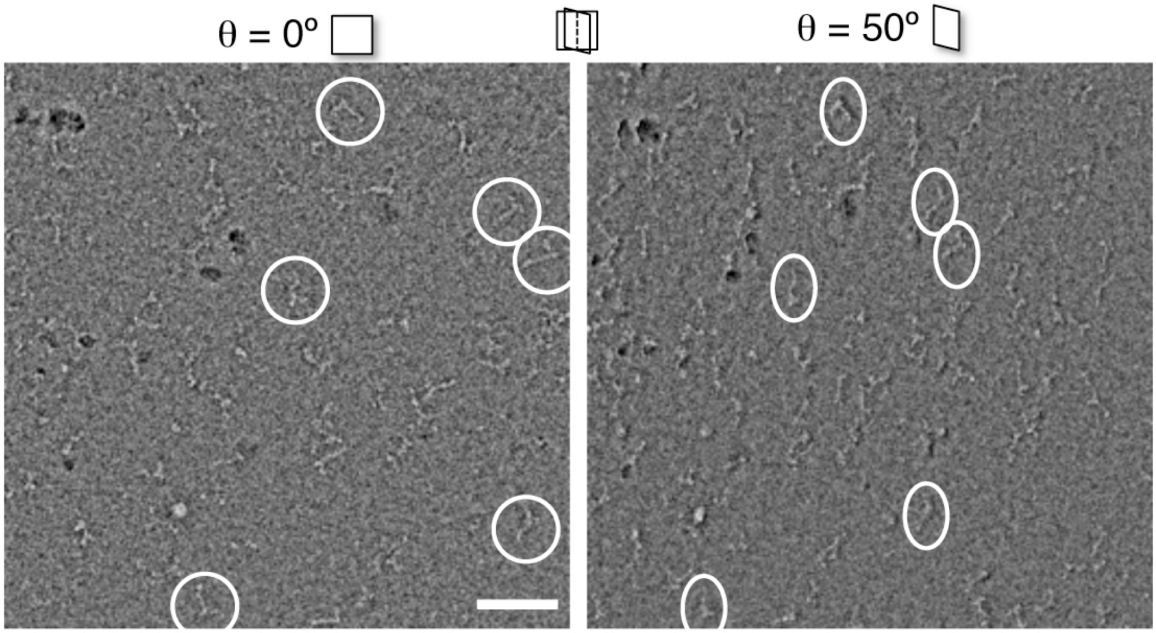

Supplementary Figure 3 Micrograph tilt pair. A field of negatively stained particles was imaged at 50º and 0º tilt. Tilt pair images of the same particle were picked as illustrated by white ovals. Scale bar, 100 nm.

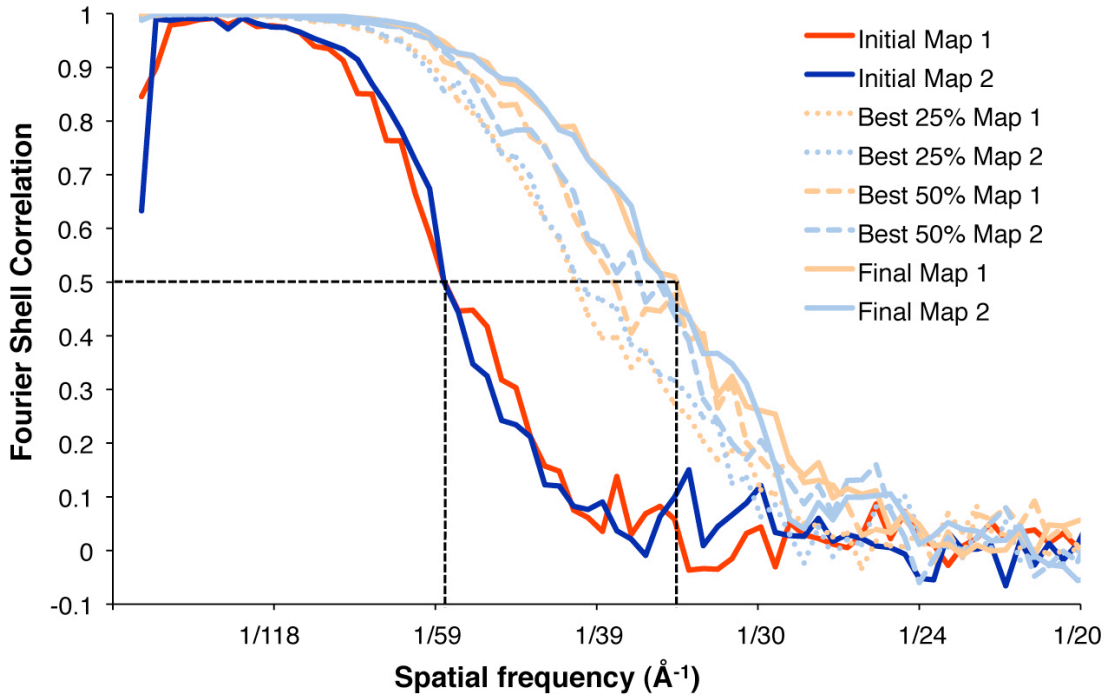

Supplementary Figure 4 Fourier Shell Correlation (FSC) for initial and final maps 1 and 2, as well as control maps that were reconstructed by projection matching, only using the best-matching 25% or 50% of particles, as shown in Supplementary Figures 5 and 6. The reproducible resolution, as defined by FSC=0.5, is ~58 Å for the initial maps and ~35 Å for the final maps.

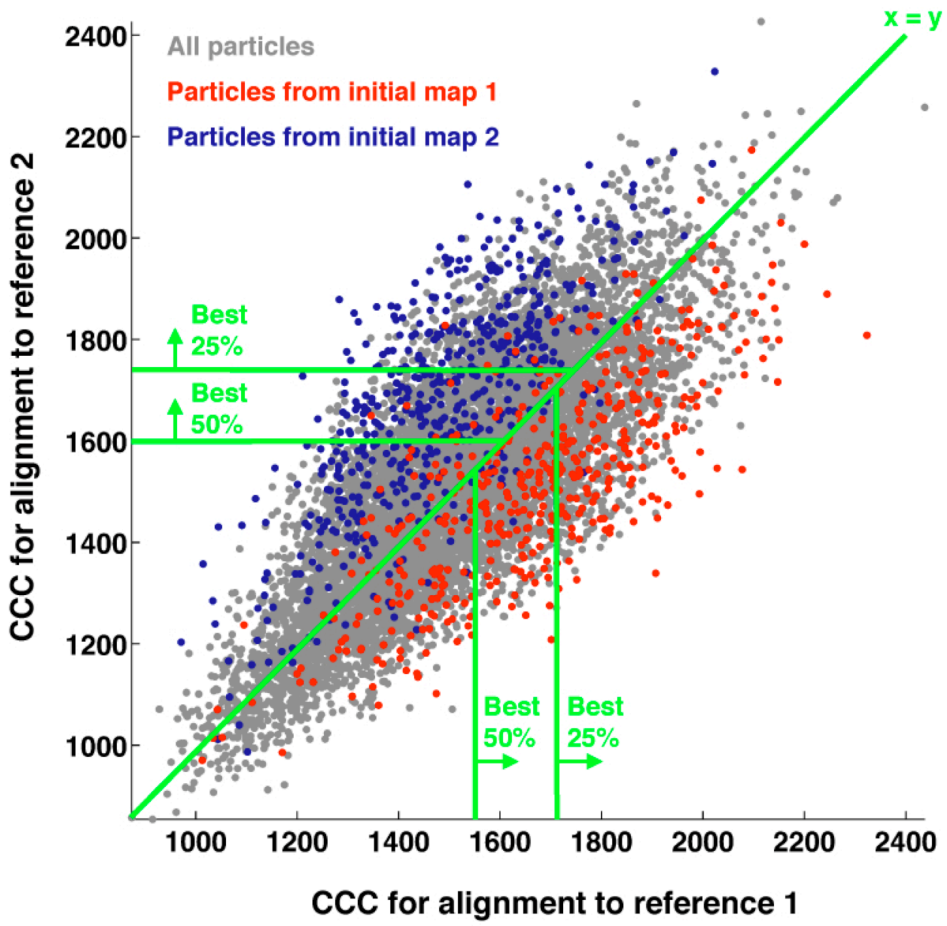

Supplementary Figure 5 Cross-correlation coefficients for projection matching. Each grey dot represents one image of a particle from the tilted specimen. The non-normalized cross-correlation coefficient between the particle and the best-matching reference projection from initial map 2 is plotted versus the non-normalized cross-correlation coefficient between the particle and the best-matching reference projection from initial map 1. Red and blue dots represent particles from the classes that were used to construct initial maps 1 and 2, respectively. The diagonal (x=y) divides the particles into two sets of particles: those that have a higher score for alignment to a projection from initial volume 1 and were used for the reconstruction of final map 1 (dots below the diagonal), and those that have a higher score for alignment to a projection from initial volume 2 and were used for the reconstruction of final map 2 (dots above the diagonal). For control purposes, volumes were also reconstructed from subsets of particles that represented the 50% or 25% of the particles in each set with the highest cross-correlation coefficients for alignment to the best reference projection.

Supplementary Figure 6

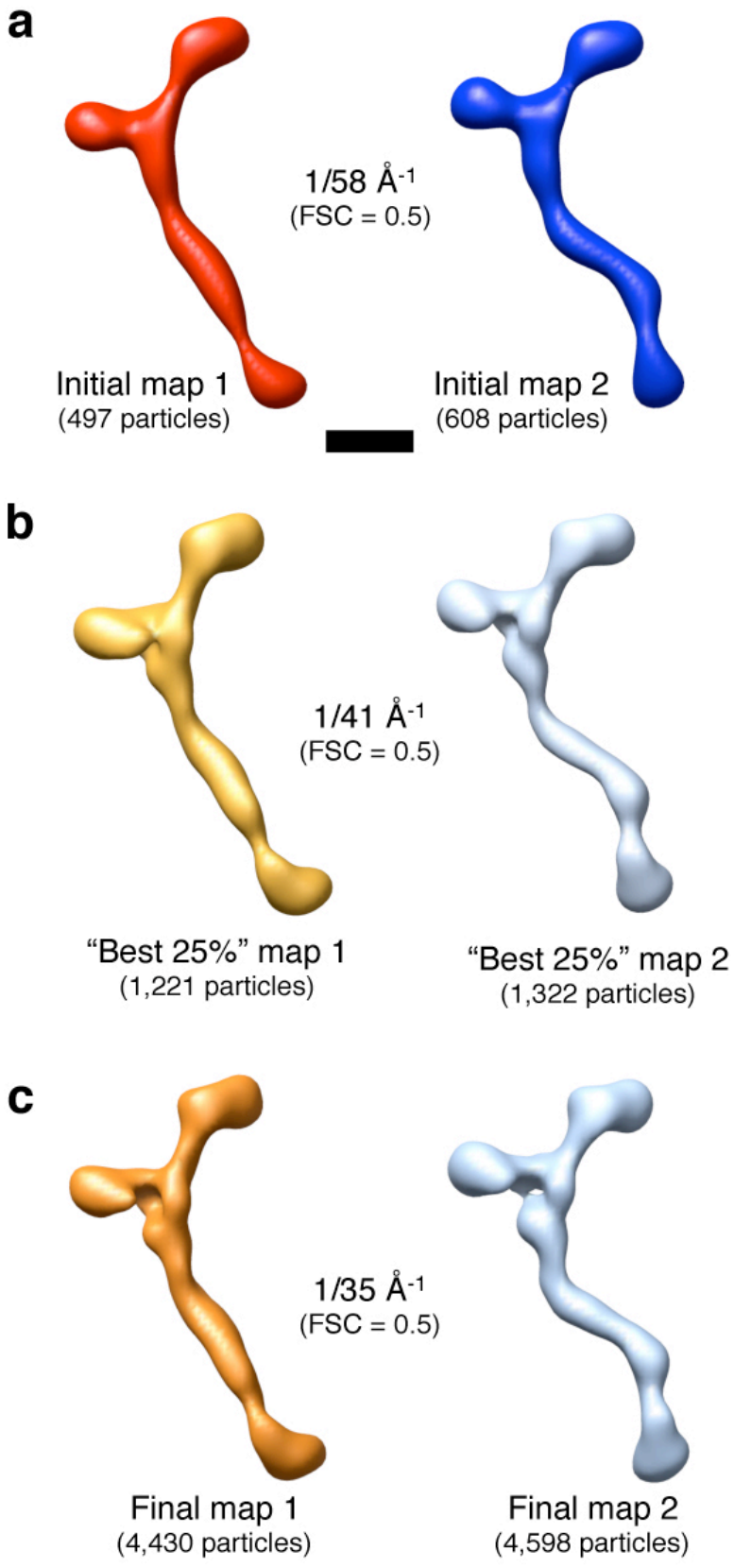

Supplementary Figure 6 Three-dimensional structures of the heptameric complex (**a**) Initial maps obtained by random-conical tilt reconstruction from the classes shown in Figure 4a (**b**) Maps obtained by projection matching and simultaneous iterative reconstruction using for each map the 25% of particles which aligned to the initial maps with the highest cross-correlation coefficients (see text for details). 4a (**c**) Final maps obtained by projection matching and simultaneous iterative reconstruction using all particles. All structures are depicted to scale as isodensity contour surfaces that were low-pass filtered beyond the reproducible resolution. Scale bar, 100 Å.

Supplementary Figure 7

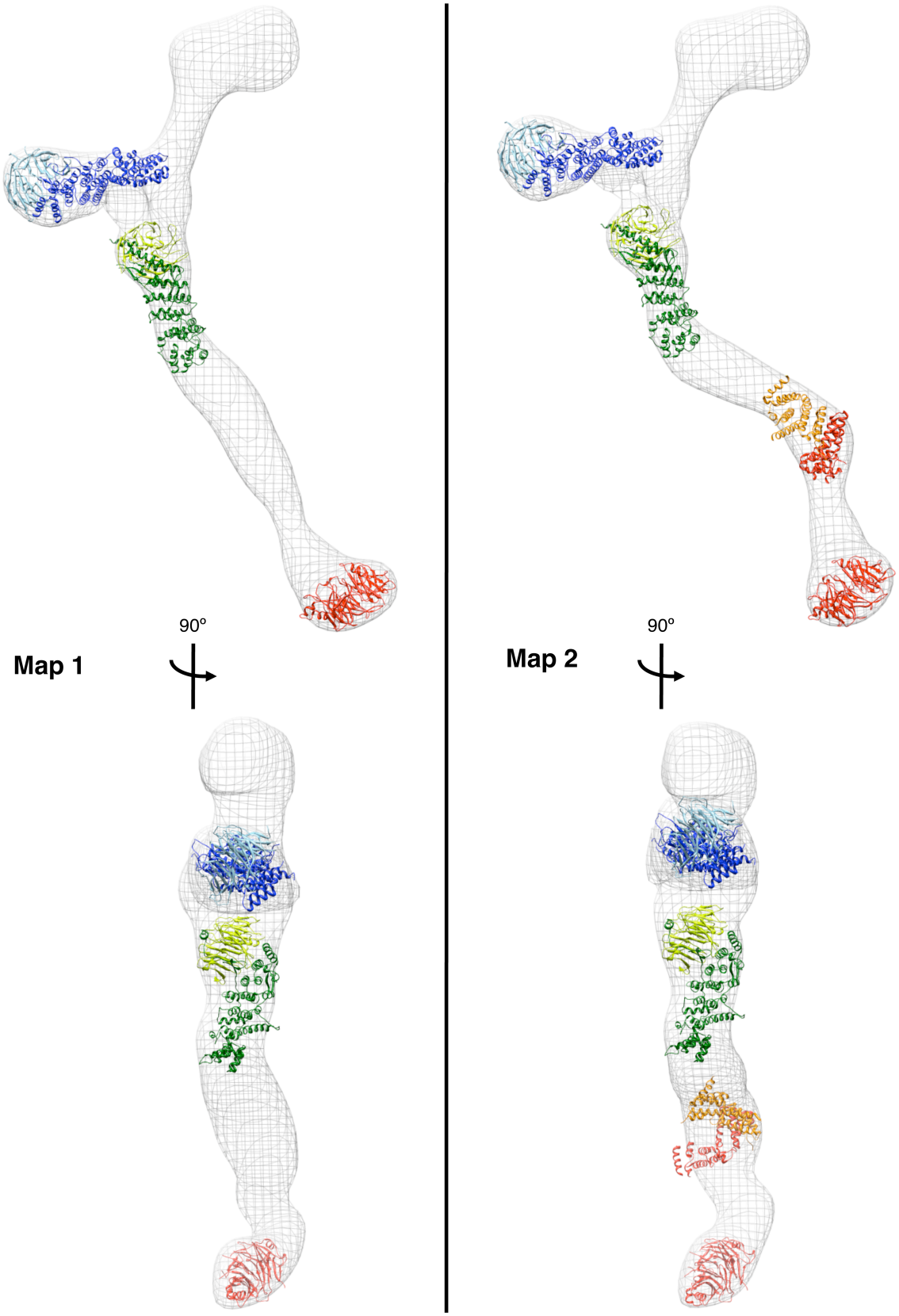

Supplementary Figure 7 Comparison of crystal structure docking into maps 1 and 2. Crystal structures were fitted computationally into maps 1 and 2 independently. Two views related by a 90º rotation around a vertical axis are shown. Color coding of crystal structures is the same as in Figure 6. Nup107·Nup133 was only docked into map 2, not map 1, since the stem hinge 2, which we showed to co-localize with the C-terminus of Nup133 (Fig. 5), is clearly visible in map 2 only. The crystal conformation of Nup107·Nup133 is likely to differ from the actual Nup84·Nup133 conformation in map 2, as evidenced by the poor fit, and the structure is included for illustrative purposes only.

SUPPLEMENTARY DISCUSSION

Projection matching

As described in the main text, initial maps were constructed from two selected particle classes using the random conical tilt method (Fig. 4a,b). We suspected that other particle images may represent slightly different views of the particle in a similar conformation. Therefore, the signal-to-noise ratio of the initial maps may be improved by incorporating additional particle images. We calculated reference projections from the two initial maps and aligned all particle images from tilted specimen to both reference projections. Supplementary Figure 5 shows the cross-correlation coefficients (CCC) for alignment of each particle to the best-matching reference projection from both initial maps (grey dots). Each particle was assigned to either map 1 or map 2 to maximize the CCC.

Red and blue dots in Supplementary Figure 5 correspond to the particles that were used to construct initial maps 1 and 2, respectively. Of the particles used for initial map 1, 86% have a higher CCC for alignment to initial map 1 projections than to initial map 2 projections; they lie below the x=y diagonal in Supplementary Figure 5. Of the particles used for initial map 2, 91% lie above the diagonal. Therefore, the CCC is a suitable criterion to distinguish the two different particle conformations.

Interestingly, the CCC distributions of particles used to reconstruct initial maps 1 and overlap with the CCC distribution of all other particles, supporting the idea that some of the other particles are likely to represent different views of a particle in the same (or a highly similar) conformation as initial maps 1 and 2.

However, the CCC distributions are unimodal; therefore, it is not possible to find by inspection a correct threshold to distinguish between particles with a conformation corresponding to the reference map and particles with a different conformation. This finding is compatible with our conclusion that there is a continuous spectrum of particle conformations.

We therefore independently reconstructed maps from three subsets for each map 1 and map 2. The subsets contained the 25% particles with the highest CCCs, the 50% particles with the highest CCCs, or all particles. The maps obtained from the

first and last of these subsets are displayed in Supplementary Figure 6. These maps are highly similar, as shown in Movies 4 and 5 (overlays of Final maps in orange and "best 25%" maps in purple for maps 1 and 2, respectively).

The Fourier shell correlation (FSC) curves for all maps are compared in Supplementary Figure 4. The reproducible resolution of the maps, as defined by FSC=0.5, increases monotonically with the number of particles used for the reconstruction. We therefore decided to use the final maps 1 and 2 (reconstructed from all particle images) for further analysis.

Localization of nups within the heptameric complex

The localization of several nups or nup complexes to different segments of the Nup84 complex was reported by Hurt and colleagues[1], and further supported by crystallographic studies[2-5]. Specifically, the following aspects of Nup84 complex architecture were previously established:

(i) Nup145C·Sec13 and Nup85·Seh1 are stable heterodimers[1] in which the seventh blade of the Sec13 and Seh1 β-propellers is contributed by Nup145C and Nup85, respectively[2-4].

(ii) Nup120 can form trimers with Nup145C·Sec13 and with Nup85·Seh1, and together, these five proteins can form a pentamer which appears in EM as a triskelion with three short arms, and can thus be concluded to correspond to the two arms and the vertex-proximal stem segment of the heptameric complex[1].

(iii) Nup84 forms a dimer with Nup133[1]; more specifically, these two nups interact via their C termini[5].

(iv) Nup133·Nup84 forms a tetramer with Nup145C·Sec13. Nup84 alone, as well as the Nup133·Nup84 dimer bind the Nup120·Nup145C·Sec13·Nup85·Seh1 pentamer, thereby extending one of the three arms into the elongated stem[1]. Taken together, these observations show that the two arms of the heptameric complex are formed by Nup120 and Nup85·Seh1, which are connected to Nup145C·Sec13 at the vertex region. Nup145C·Sec13 forms the upper part of the stem, Nup84 the mid-stem and Nup133 the distal stem and the foot.

This assignment does not establish the identity of the short and the long arm. We therefore mapped the position of Seh1 by EM and found it to localize to the short arm of the heptamer. We also mapped the position of the Nup133 C terminus, which localized to the stem hinge 2 region.

Details of crystal structure docking within the EM maps

The Nup85·Seh1 dimer assumed highly similar orientations in EM maps 1 and 2 (Supplementary Fig. 7). The crystal structure of Nup85 lacks 174 C-terminal amino acids. The C terminus of the crystallized Nup85 fragment points towards the end of the short arm (Fig. 6c, Supplementary movie 3). Since the end of the short arm is occupied with the Seh1 β-propeller, additional C-terminal residues of Nup85 likely fold back towards the vertex region. The crystallized domain of Nup85 does not completely fill the short arm of the EM map, thus leaving space for the Nup85 C terminus. However, the current resolution of the EM map is not sufficient to discern the exact location of the additional residues.

The Nup145C·Sec13 dimer also had highly similar orientations in maps 1 and 2 (Supplementary Fig. 7). The crystal structure of Nup145C lacks 125 N-terminal amino acids and 156 C-terminal amino acids. Both the N and C terminus of the crystallized Nup145C fragment point towards the vertex of the heptamer (Fig. 6d, Supplementary movie 3), suggesting that the region between the knob and the vertex is filled with the remaining portions of Nup145C.

The N-terminal Nup133 β-propeller docked into the foot regions of maps 1 and 2 in similar orientations (Fig. 6e, Supplementary Figure 7). The C terminus of the crystallized Nup133 β-propeller domain points away from the stem; the following residues will have to fold back to connect to the remaining part of Nup133. Again, the resolution of the EM map is not high enough to predict the exact path taken by protein fragments absent from the crystal structure.

The global fitting method failed for the Nup107·Nup133 structure: none of the computed positions coincided with stem hinge 2. Therefore, we positioned the crystal structure manually in this region and optimized the local fit computationally.

SUPPLEMENTARY REFERENCES

1. Lutzmann, M., Kunze, R., Buerer, A., Aebi, U. & Hurt, E. Modular self-assembly of a Y-shaped multiprotein complex from seven nucleoporins. *EMBO J* **21**, 387-97 (2002).

2. Hsia, K.C., Stavropoulos, P., Blobel, G. & Hoelz, A. Architecture of a coat for the nuclear pore membrane. *Cell* **131**, 1313-26 (2007).

3. Debler, E.W. et al. A fence-like coat for the nuclear pore membrane. *Mol Cell* **32**, 815-826 (2008).

4. Brohawn, S.G., Leksa, N.C., Spear, E.D., Rajashankar, K.R. & Schwartz, T.U. Structural evidence for common ancestry of the nuclear pore complex and vesicle coats. *Science* **322**, 1369-73 (2008).

5. Boehmer, T., Jeudy, S., Berke, I.C. & Schwartz, T.U. Structural and functional studies of Nup107/Nup133 interaction and its implications for the architecture of the nuclear pore complex. *Mol Cell* **30**, 721-31 (2008).